DOI: 10.48011/asba.v2i1.1101

Machine Learning Techniques for Fault Diagnosis of Rotating Machines Using Spectrum Image of Vibration Orbits

Clayton Eduardo Rodrigues [*]
Cairo Lúcio Nascimento Júnior [**] **Domingos Alves Rade** [***]

[*] *Instituto Tecnológico de Aeronáutica - ITA, SP (claytonr@ita.br)*
[**] *Instituto Tecnológico de Aeronáutica - ITA, SP (cairo@ita.br)*
[***] *Instituto Tecnológico de Aeronáutica - ITA, SP (rade@ita.br)*

Abstract: A comparative analysis of machine learning techniques for rotating machine faults diagnosis based on vibration spectra images is presented. The feature extraction of different types of faults, such as unbalance, misalignment, shaft crack, rotor-stator rub, and hydrodynamic instability, is performed by processing the spectral image of vibration orbits acquired during the rotating machine run-up. The classifiers are trained with simulation data and tested with both simulation and experimental data. The experimental data are obtained from measurements performed on an rotor-disk system test rig supported on hydrodynamic bearings. To generate the simulated data, a numerical model of the rotating system is developed using the Finite Element Method (FEM). Deep learning, ensemble and traditional classification methods are evaluated. The ability of the methods to generalize the image classification is evaluated based on their performance in classifying experimental test patterns that were not used during training. The obtained results suggest that despite considerable computational cost, the method based on Convolutional Neural Network (CNN) presents the best performance for classification of faults based on spectral images.

Keywords: rotating machine, diagnosis, spectral image, vibration, machine learning

1. INTRODUCTION

Rotating machines such as pumps, motors and electric generators, turbines, compressors, and industrial fans are widely used in the industry. In order to reduce the risk of damage and possible failure of such equipment, fault diagnostic methods are frequently applied. Generally, fault diagnosis consists of two steps: feature extraction and fault classification (Liu et al., 2018; Jardine et al., 2006).

As an abnormal condition of rotating machinery is most frequently accompanied by changes in vibration patterns, faults can be detected by extracting the features of vibration signals. In the literature, traditional feature extraction methods include time domain, frequency domain, and time-frequency domain methods (Bin et al., 2012; Chandra and Sekhar, 2016; Li et al., 2015).

Time domain methods deal directly with the waveform by applying filters or extracting features that include the mean, standard deviation, Root Mean Square (RMS), crest factor, and kurtosis factor (Jardine et al., 2006).

In the frequency domain, the most traditional and widely used method is the Fast Fourier Transform (FFT). Other important method is the spectrum of orbits formed by vibration signals measured in two mutually orthogonal directions, known as Full Spectrum (Goldman and Muszynska, 1999; Southwick, 1994; Laws, 1998; Southwick, 1993).

Time-frequency methods are combinations of time and frequency domain methods. This category of method is used to analyze signals from non-stationary waveforms. Short Time Fourier Transforms (STFT) and the Wavelet Transform (WT) are among the most popular methods. Comparative studies can be found in Chandra and Sekhar (2016).

As the Full Spectrum is recognized to provide more information than traditional frequency spectrum, it allows to detect the symptoms of some types of failure. It can be used for steady state analysis or for transient analysis by means of the Full Spectrum Cascade plot, formed by a series of time-indexed spectra obtained during the machine run-up or run-down (Muszynska, 2005).

Investigation of dynamic behavior and fault diagnosis using the transient response of a machine has attracted interest of many researchers due to the fact that it provides superior performance when compared to the use of steady state response (Chandra and Sekhar, 2016; Wei et al., 2019).

Recently, researchers have employed image processing methods to perform automatic feature extraction and fault diagnosis in a two-dimensional space. According to Ciabattoni et al. (2018); Lu et al. (2016); Amar et al. (2015); Jeong et al. (2016), two-dimensional pattern classification techniques have proven to be a powerful tool for rotary machine fault diagnosis.

Classification methods, such as Convolutional Neural Network (CNN), Support Vector Machine (SVM), k-Nearest Neighbors (kNN), and Multiple Classifier System (MCS) or ensemble, have been proposed for image classification. Some classification approaches have focused on designing an effective dimension reduction technique, such as Principal Component Analysis (PCA), Independent Component Analysis (ICA), and autoencoder (AE) (Ng, 2017; Lin et al., 2013).

The topic of the present study is the identification of unbalance, misalignment, transverse shaft crack, rotor-stator rub, and hydrodynamic instability faults in rotating machinery, based on vibration responses. The fault feature extraction is performed by processing the spectral image of orbits in run-up vibration response. Promising fault classification methods based in image processing are evaluated. The modeling of an experimental rotor-bearing system with faults is performed using Finite Element Method (FEM). Fault modeling allows to study the dynamic behavior of the rotary system under controlled parameters such as location and magnitude of faults. In addition, this enables to avoid exhaustive work to obtain the amount of data needed to train the classifiers. The classifiers are trained with data obtained from computer-simulated data and tested with both computational and experimental data sets. Thus, the generalization capability of the classifiers can be well investigated.

In Section 3, the FEM of the rotor-bearing system with faults is presented. The main theoretical foundations for fault feature extraction that underlie this work are presented in Section 4. In Section 5, simulation and experimental fault image processing, and classifier performance, are presented followed by conclusions in Section 6.

2. PROPOSED METHOD

The proposed fault diagnosis procedure is showed schematically in Fig.1. It comprises five major steps:

- Acquisition of transverse vibration signals in two orthogonal directions and the corresponding rotating speed, during run-up of the machine.
- Computation of the Full Spectrum Cascade plot of the vibration signals.
- Image construction with normalization and reduction of image resolution. Maximum filter is applied to reduce the resolution to 30x30 pixels.
- Dimension reduction using PCA or AE required for classic classification methods. kNN, SVM and Random Forest (RF).
- Fault classification. CNN, kNN, Random Subspace ensemble for kNN (RS kNN), SVM, and RF classification methods are proposed for this research work.

3. MODELING OF ROTATING SYSTEM WITH FAULTS

A typical rotating system consists of a flexible shaft supported by bearings. Disks are disposed along the shaft. For the FEM modeling, the formulation presented in Friswell et al. (2010) is followed. Timoshenko's beam element theory is used to model the shaft, including the effects of transverse shear deformation, rotary inertia and

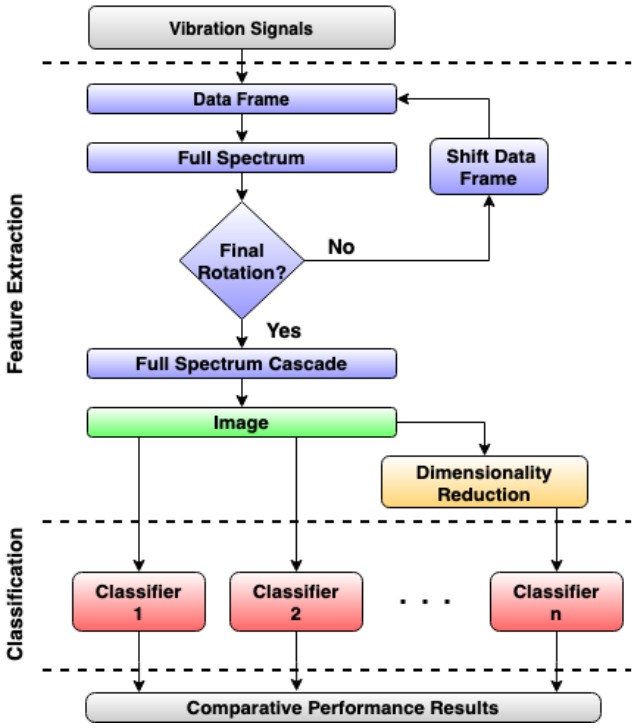

Figure 1. The proposed fault diagnosis scheme.

gyroscopic moments. The disks are assumed to be rigid, and the bearings are of the hydrodynamic type, which means that forces are transmitted between the fixed and rotating parts of the bearing through a an oil film.

The global finite element model of the rotor-bearing system with the faults represented by forces exercised on the rotor is written as follows Friswell et al. (2010); Lalanne and Ferraris (2001):

$$\begin{bmatrix}\dot{\mathbf{q}}\\ \ddot{\mathbf{q}}\end{bmatrix} = \begin{bmatrix}\mathbf{0} & \mathbf{I}\\ -\mathbf{M}^{-1}\mathbf{K} & -\mathbf{M}^{-1}(\mathbf{C}+\Omega\mathbf{G})\end{bmatrix}\begin{bmatrix}\mathbf{q}\\ \dot{\mathbf{q}}\end{bmatrix} + \begin{bmatrix}\mathbf{0}\\ \mathbf{M}^{-1}\mathbf{f}\end{bmatrix} \tag{1}$$

where,

$$\mathbf{f} = \mathbf{f}^g + \mathbf{f}^u + \mathbf{f}^b + \mathbf{f}^m + \mathbf{f}^r + \mathbf{f}^c. \tag{2}$$

In Eq. $\mathbf{q}, \dot{\mathbf{q}}, \ddot{\mathbf{q}}$ denote, respectively, the vectors of nodal displacements and rotations, and corresponding velocities and accelerations. In addition, (1), $\mathbf{M}$ is the global mass matrix, $\mathbf{C}$ is the global damping matrix, $\mathbf{G}$ is the global gyroscopic matrix, $\mathbf{K}$ is the global stiffness matrix and Ω is the rotational speed. In Eq. 2, the vector $\mathbf{f}$ is composed of the following forces applied to the shaft: gravitational force $\mathbf{f}^g$; unbalance force $\mathbf{f}^u$; forces applied by the bearings $\mathbf{f}^b$ (Adiletta et al., 1996); misalignment force $\mathbf{f}^m$ (Sekhar and Prabhu, 1995); rub force $\mathbf{f}^r$ (Han et al., 2008); and shaft crack force $\mathbf{f}^c$ (Papadopoulos and Dimarogonas, 1987; Mayes and Davies, 1984; Sekhar and Prabhu, 1992).

4. FEATURE EXTRACTION BASED ON ORBIT SPECTRUM

The vibration orbit at a given point of the rotor-bearing can be expressed as the vector sum of the harmonic components of vibration in the x and y directions in the complex plane:

$$c(t) = x(t) + jy(t), \tag{3}$$

where $j = \sqrt{-1}$.

The full spectrum is calculated by the discrete Fourier transform of the vibration orbit. The time signals appearing in (3) are first converted into their discrete-time representations $x(n)$, $y(n)$, and the complex coefficients which contains the amplitude and phase of the orbit vector is computed as follows:

$$c(k) = \sum_{n=0}^{N-1} [x(n)e^{-j\frac{2\pi}{N}nk} + jy(n)e^{-j\frac{2\pi}{N}nk}], \tag{4}$$

where, $k = 0, ..., N-1$.

Fig. 2 shows a typical Full Spectrum Cascade plot obtained from a run-up rotating machine. This plot is obtained adding rotational speed axis to the Full Spectrum plot. This third dimension, together with frequency and vibration amplitude dimensions, is obtained positioning the Full Spectrum's in the order of increasing rotational speed. Each baseline of plotted Full Spectrum corresponds to the rotational speed. Forward (1X and 2X) and reverse (-1X and -2X) components are shown, where, 1X and 2X are forward components with the same frequency and with the double frequency of rotation speed, respectively.

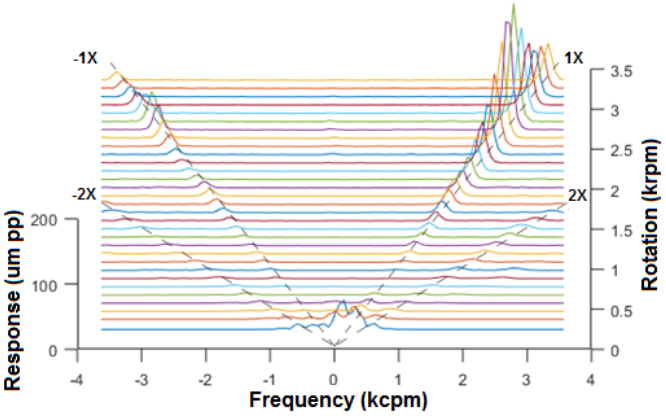

Figure 2. Typical full spectrum cascade plot.

5. RESULTS

5.1 Computational simulation

Computational simulations of a rotor-bearing system were performed on a finite element model intended to represent the test bench depicted in Fig. 3. The rotor system with a flexible shaft has one disk and is supported by two identical hydrodynamic bearings. Cylinder sleeves aligned with the vibration sensors were modeled as small disks. The sleeves were installed on the experimental rotor shaft in order to reduce measurement noise caused by electromagnetic interference between the sensors. The geometry and details of the finite element model are shown in Fig. 4, while the properties of the rotor-bearing system are given in Table 1. Vibration response of the shaft is acquired at nodes 5 and 17 in the horizontal and vertical directions.

In order to get training data that broadly span the problem data space, random variations with uniform distribution of

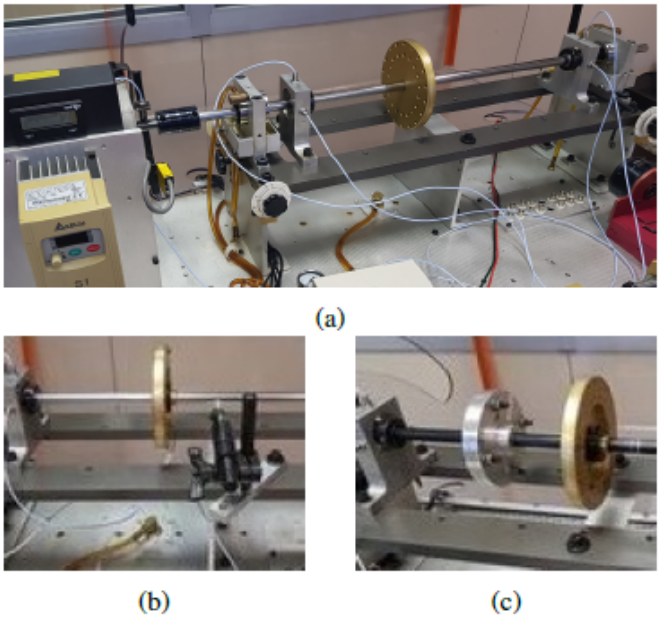

Figure 3. Experimental test bench. (a) Rotor-bearing test bench. (b) Rotor-stator rub setup. (c) Crack shaft setup.

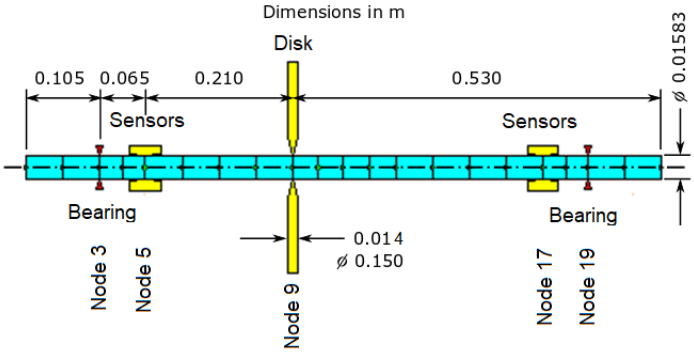

Figure 4. Finite element model and geometry of rotor-bearing system.

the some model parameters were performed. The chosen model parameters and distribution limits with respect to the nominal values were defined for each type of fault. In addition, the simulations distributed in the same quantity at nodes 7, 9, 11, 13 and 15. The full spectrum cascade plots for each fault type. which are described next, are shown in Figs. 5 to 9.

Unbalance A disk unbalance mass of 1.02 g, located 5cm from the centerline of the rotor shaft, was considered for unbalance fault simulation with the following range of random variations: unbalance mass from -35% to +5%; damping factor from -30% to +30%; bearing clearance from -20% to +20%; disk thickness from -20% to +20%.

Misalignment For the rotor-bearing system with angular misalignment, the following variations are considered: unbalance mass from -35% to +5%; damping factor from -30% to +30%; bearing clearance from -20% to +20%; disk thickness from -20% to +20%; and angular misalignment from 0.006° to 0.02°.

Table 1. Properties of the rotor-bearing system

Parameter	Value
Shaft	
Length	0.91 m
Diameter	15.83×10^{-3} m
Density	7800 kg/m^3
Modulus of elasticity	2.11×10^{11} N/m^2
Poisson's coefficient	0.3
Damping factor	8×10^{-5}
Disk	
External diameter	0.15 m
Internal diameter	15.83×10^{-3} m
Width	14.0×10^{-3} m
Density	2697 kg/m^3
Sleeve	
External diameter	32×10^{-3} m
Internal diameter	15.83×10^{-3} m
Width	43.5×10^{-3} m
Density	7800 kg/m^3
Hydrodynamic Bearing	
Length (L)	6.5×10^{-3} m
Diameter (D)	15.96×10^{-3} m
Clearance	64.0×10^{-6} m
Dynamic viscosity	0.1398 Pa s

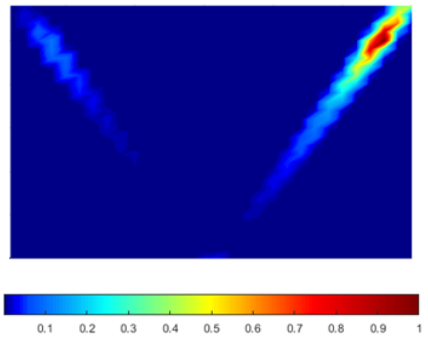

Figure 5. Image of a typical simulated full spectrum cascade plot for the rotating machine with unbalance.

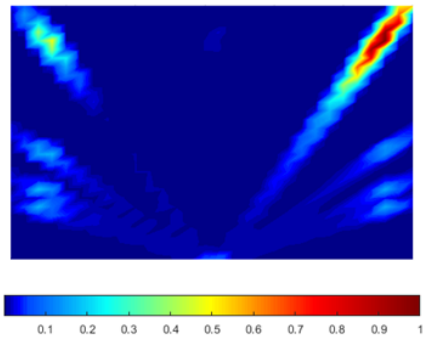

Figure 6. Image of a typical simulated full spectrum cascade plot for the rotating machine with misalignment.

Rubbing For the rotor-bearing system subjected to rotor-stator rubbing, the following variations were considered: stator clearance from 30% to 50% of the difference between final and maximum values of vibration in x axis, at node 11; unbalance from -5% to +5%; damping factor from -30% to +30%; bearing clearance from -20% to +20%; and disk thickness from -20% to +20%.

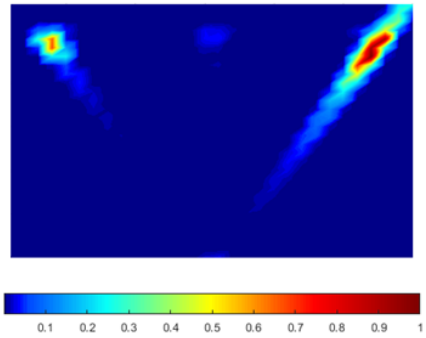

Figure 7. Image of a typical simulated full spectrum cascade plot for the rotating machine with rotor-stator rubbing.

Shaft crack In this case, the following variations were considered: unbalance from -35% to +5%; damping factor from -30% to +30%; bearing clearance from -20% to +20%; disk thickness from -20% to +20%; and crack from 50% to 65% of the shaft radius.

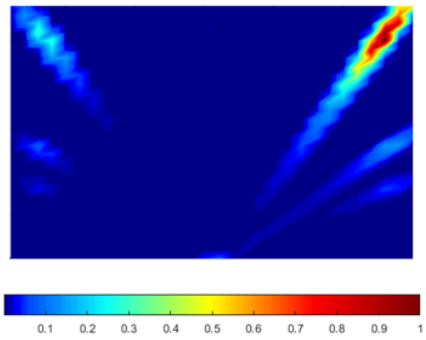

Figure 8. Image of a typical simulated full spectrum cascade plot for the rotating machine with a shaft crack.

Hydrodynamic instability In this simulation, the rotor weight is removed and dynamic oil viscosity reduced to 0,0093 Pa.s; variation of unbalance simulation from -32% to -18%; damping factor from -5% to +5%; bearing clearance from -5% to 5%; and disk thickness from -5% to +5%.

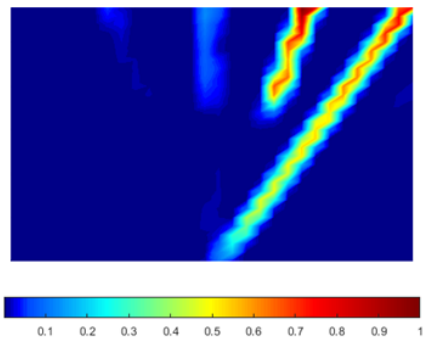

Figure 9. Image of a typical simulated full spectrum cascade plot for the rotating machine presenting hydrodynamic instability.

As can be seen in Fig. 6, misalignment lead to increase of both forward and reverse components (2X, 3X, 4X, -2X, -3X and -4X), whereas the shaft crack, showed in Fig. 8, promotes predominantly increase of the forward components (2X and 3X). The significant influence of rubbing is observed with increases of reverse component (-1X) at critical speed, as presented in Fig. 7. In Fig. 9, hydrodynamic instability is evidenced by the presence of forward subsynchronous components (about 0.48X). In the presence of unbalance (Fig. 5), predominantly only forward 1X component is increased.

5.2 Experimental tests

As in Section 5.1, the experimental measurements were acquired at positions corresponding to nodes 7, 9, 11, 13 and 15. An image of the full spectrum obtained for the rotating machine under each fault type is shown in Figs. 10 to 14.

Unbalance In addition to changing the position of the disk, some experiments were performed with residual unbalance while others were conducted with a mass of 1.02 g, located 5 cm from the centerline of the rotor shaft.

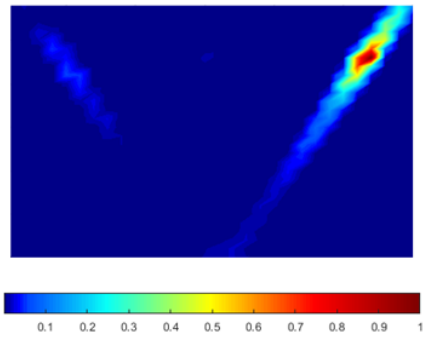

Figure 10. Image of an experimental full spectrum cascade plot for the rotating machine with unbalance.

Misalignment The value of the angular misalignment is between 0.15° and 0.4°.

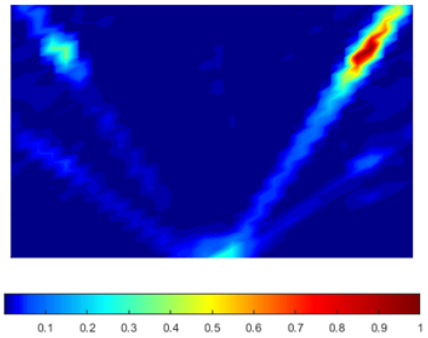

Figure 11. Image of an experimental full spectrum cascade plot for the rotating machine presenting with misalignment.

Rubbing Stator clearance is adjusted for rubbing when rotor rotation passes through critical speed.

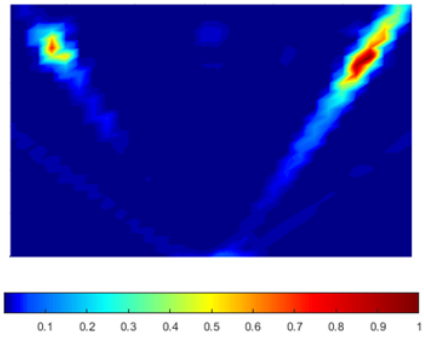

Figure 12. Image of an experimental full spectrum cascade plot for the rotating machine presenting rotor-stator rubbing.

Shaft crack Using two shafts connected by flanges, the experiments were performed by adjusting the tightness of two adjacent flange screws. Part of the experiments were performed with residual unbalance and part with the additional unbalance mass installed on the disk at different angular positions.

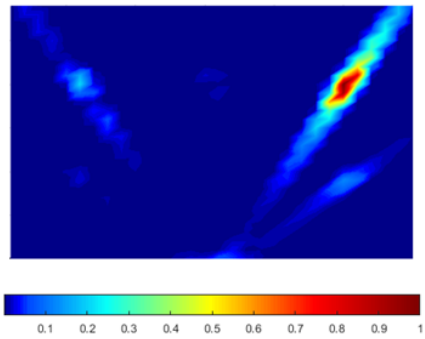

Figure 13. Image of an experimental full spectrum cascade plot for the rotating machine presenting a shaft crack.

Hydrodynamic Instability The experiments were performed with a bearing with longer length (length/diameter ratio = 1).

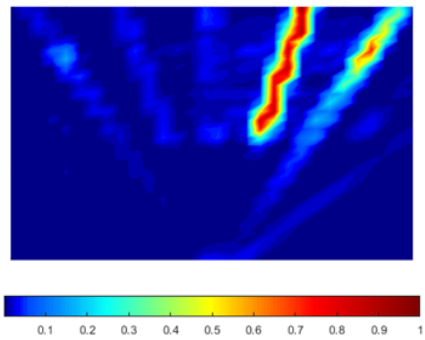

Figure 14. Image of an experimental full spectrum cascade plot for the rotating machine with hydrodynamic instability.

5.3 Classification performance

Table 2 describes all of the images obtained from numerical simulations and experimental tests. Out of 1250 simulation images, 1125 were used for training and 125 for fault classification test. k-fold cross-validation is performed with k=10. In addition, all the 150 experimental images were used for test.

Table 2. Number of simulated and experimental full spectrum images.

Simulated Image (10-Fold Cross-Validation)		**Experimental Image**	**Total**
Train	***Test***	***Test***	
1125	125	150	1400

The means (μ) of the accuracies and the computational costs of the fault classifications methods with their respectives standard deviations (σ) are presented in Table 3. The entire development was performed with a computer code written in environment MATLAB, version R2018b, run on microcomputer having an Intel Core i7 processor.

The best configuration found for each classifier proposed in this work are:

- CNN: first convolution layer: 32 filters 3×3, activation function ReLU, maxpooling 2 × 2, stride 2; second convolution layer: 56 filters 4 × 4, activation function ReLU, maxpooling 3 × 3, stride 1; fully connected layer: 5 neurons; dropout: 0.5.
- RS kNN: number of subspaces: 450; number of estimators: 30.
- PCA kNN: principal components: 12; distance measure: cosine; number of neighbors: 1.
- PCA SVM: principal components: 19; Kernel function: gaussian; C: 0.7; γ: 1.
- AE SVM: hidden layer size: 150; regularization: 1 (sparsity) and 0.001 (L2 weight); proportion (sparsity): 0.3; Kernel function: RBF.
- PCA RF: principal components: 19; number of estimators: 40, meta-algorithm: bagging.

Table 3. Fault Classification Results

Method	**Simulation Data**						**Experimental Data**	
	Train Time(s)		***Test Time(s)***		***Test Acc(%)***		***Test Acc(%)***	
	μ	σ	μ	σ	μ	σ	μ	σ
CNN	77.5	1.8	0.16	0.01	92.7	2.0	88.7	3.6
RS kNN	0.59	0.07	0.03	0.01	91.6	3.1	66.2	4.1
PCA kNN	0.57	0.60	0.03	0.01	85.8	4.2	75.5	2.8
PCA SVM	0.72	0.07	0.04	0.01	78.8	4.0	70.3	1.5
AE SVM	97.5	0.6	0.03	0.01	73.0	2.5	71.9	2.3
PCA RF	1.12	0.10	0.06	0.01	93.0	1.7	66.0	6.2

The results of Table 3 showed that the CNN classification method presented the best performance, reaching 88.7% test accuracy for the experimental data set. Despite the PCA with Random Forest method reached 93.0% accuracy in the test with simulation data, it reached only 66.0% in the test with experimental data, indicating that has been over-fitted, this method showed poorly performance than other proposed classifiers.

As the execution time can measure the computational cost of an algorithm (Ascencio and de Araújo, 2010), the execution times of the proposed methods with the simulation data set showed that the AE SVM classification method presented highest computational cost, with an execution time of 97.5 s for training, followed by CNN with 77.5 s. On the other hand, the PCA kNN classification method showed the lowest computational cost, consuming only 0.57 s of training execution time.

Confusion matrices were created (Tables 4 and 5) to check which classes or faults were confused in the respective classification methods. The matrix columns indicate the true classes while the lines indicate the estimated classes. Each element of the matrix corresponds to the number of images of a true class that was assigned to the estimated class. At the bottom of the matrix is the result of calculating the effectiveness for the classification of each fault, this metric is generally known as Recall (Sokolova and Lapalme, 2009). An acronym was assigned to each fault, namely: (SC) shaft crack, (HI) hydrodynamic instability, (MA) misalignment, (RU) rubbing and (UB) unbalance.

Table 4. Confusion matrix of the experimental test with CNN (88.7% accuracy).

	True Values				
	SC	HI	MA	RU	UB
SC	**294**	29	45	0	49
HI	0	**255**	4	0	0
MA	6	0	**232**	0	0
RU	0	12	18	**300**	1
UB	0	4	1	0	**250**
	98%	85%	77%	100%	83%

Table 5. Confusion matrix of the experimental test with PCA kNN (75.5% accuracy).

	True Values				
	SC	HI	MA	RU	UB
SC	**248**	40	82	32	72
HI	0	**260**	0	0	0
MA	20	0	**130**	0	1
RU	0	0	43	**268**	0
UB	32	0	45	0	**227**
	83%	87%	43%	89%	76%

The confusion matrices obtained with the experimental data set showed that misalignment was one of the faults with the highest number of false negatives, with the prediction rates 77% for CNN and 43% for PCA kNN, indicating low efficiency of the classifiers for the identification of this type of fault. Based on these results, it can be seen that among the models of the simulated faults, misalignment was the one that presented the lowest fidelity in relation to the respective fault tested at the experimental bench, since the training data did not cover all the data space of the respective experiment.

6. CONCLUSIONS

Considering that spectral analysis of full spectrum cascade plots is a powerful method used to identify the condition of the rotating machine, an autonomous diagnostic system based in spectral image extracted from these plots was developed to identify a group of faults of interest.

According to the results, the classification method based in CNN presented greater generalization capacity than

the other proposed methods, since this method presented higher accuracy rate in tests with experimental data.

The lowest computational costs were found in the classifiers combined with the reduction of dimensionality by the PCA method. A relevant highlight is the PCA kNN classifier, which, in spite of showing performance inferior to CNN, presented a satisfactory performance at the lowest computational cost.

ACKNOWLEDGMENTS

D.A. Rade gratefully acknowledges the funding provided by Fundação de Amparo à Pesquisa do Estado de São Paulo - FAPESP (grant #2015/20363-6).

REFERENCES

Adiletta, G., Guido, A.R., and Rossi, C. (1996). Chaotic motions of a rigid rotor in short journal bearings. *Nonlinear Dynamics*, 10(3), 251–269.

Amar, M., Gondal, I., and Wilson, C. (2015). Vibration spectrum imaging: A novel bearing fault classification approach. *IEEE Transactions on Industrial Electronics*, 62(1), 494–502. doi:10.1109/tie.2014.2327555.

Ascencio, A.F.G. and de Araújo, G.S. (2010). *Estruturas De Dados: algoritmos, análise da complexidade e implementação em JAVA e C/C++*. PEARSON BRASIL.

Bin, G.F., Gao, J.J., Li, X.J., and Dhillon, B.S. (2012). Early fault diagnosis of rotating machinery based on wavelet packets—empirical mode decomposition feature extraction and neural network. *Mechanical Systems and Signal Processing*, 27, 696–711. doi:10.1016/j.ymssp.2011.08.002.

Chandra, N.H. and Sekhar, A.S. (2016). Fault detection in rotor bearing systems using time frequency techniques. *Mechanical Systems and Signal Processing*, 72-73, 105–133. doi:10.1016/j.ymssp.2015.11.013.

Ciabattoni, L., Ferracuti, F., Freddi, A., and Monteriu, A. (2018). Statistical spectral analysis for fault diagnosis of rotating machines. *IEEE Transactions on Industrial Electronics*, 65(5), 4301–4310. doi:10.1109/tie.2017.2762623.

Friswell, M.I., Penny, J.E.T., Garvey, S.D., and Lees, A.W. (2010). *Dynamics of rotating machines*. Cambridge University Press, New York.

Goldman, P. and Muszynska, A. (1999). Application of full spectrum to rotating machinery diagnostics. *Orbit*, 20(1), 17–21.

Han, Q., Zhang, Z., and Wen, B. (2008). Periodic motions of a dual-disc rotor system with rub-impact at fixed limiter. *Proceedings of the Institution of Mechanical Engineers, Part C: Journal of Mechanical Engineering Science*, 222(10), 1935–1946.

Jardine, A.K.S., Lin, D., and Banjevic, D. (2006). A review on machinery diagnostics and prognostics implementing condition-based maintenance. *Mechanical Systems and Signal Processing*, 20(7), 1483–1510.

Jeong, H., Park, S., Woo, S., and Lee, S. (2016). Rotating machinery diagnostics using deep learning on orbit plot images. *Procedia Manufacturing*, 5, 1107–1118. doi:10.1016/j.promfg.2016.08.083.

Lalanne, M. and Ferraris, G. (2001). *Rotordynamics prediction in engineering*. Wiley, Chichester, 2 edition.

Laws, B. (1998). When you use spectrum, don't use it halfway. *Orbit*, 18(2).

Li, W., Zhu, Z., Jiang, F., Zhou, G., and Chen, G. (2015). Fault diagnosis of rotating machinery with a novel statistical feature extraction and evaluation method. *Mechanical Systems and Signal Processing*, 50-51, 414–426. doi:10.1016/j.ymssp.2014.05.034.

Lin, Z., Chen, Y., Zhao, X., and Wang, G. (2013). Spectral-spatial classification of hyperspectral image using autoencoders. In *2013 9th International Conference on Information, Communications & Signal Processing*. IEEE. doi:10.1109/icics.2013.6782778.

Liu, R., Yang, B., Zio, E., and Chen, X. (2018). Artificial intelligence for fault diagnosis of rotating machinery: A review. *Mechanical Systems and Signal Processing*, 108, 33–47. doi:10.1016/j.ymssp.2018.02.016.

Lu, C., Wang, Y., Ragulskis, M., and Cheng, Y. (2016). Fault diagnosis for rotating machinery: A method based on image processing. *PLOS ONE*, 11(10). doi:10.1371/journal.pone.0164111.

Mayes, I.W. and Davies, W.G.R. (1984). Analysis of the response of a multi-rotor-bearing system containing a transverse crack in a rotor. *Journal of Vibration Acoustics Stress and Reliability in Design*, 106(1), 139. doi:10.1115/1.3269142.

Muszynska, A. (2005). *Rotordynamics*. CRC Press, Flórida, 1 edition. doi:10.1201/9781420027792.

Ng, S.C. (2017). Principal component analysis to reduce dimension on digital image. *Procedia Computer Science*, 111, 113–119.

Papadopoulos, C.A. and Dimarogonas, A.D. (1987). Coupled longitudinal and bending vibrations of a rotating shaft with an open crack. *Journal of Sound and Vibration*, 117(1), 81–93. doi:10.1016/0022-460x(87)90437-8.

Sekhar, A.S. and Prabhu, B.S. (1992). Crack detection and vibration characteristics of cracked shafts. *Journal of Sound and Vibration*, 157(2), 375–381. doi:10.1016/0022-460x(92)90690-y.

Sekhar, A.S. and Prabhu, B.S. (1995). Effects of coupling misalignment on vibrations of rotating machinery. *Journal of Sound and Vibration*, 185(4), 655–671. doi:10.1006/jsvi.1995.0407.

Sokolova, M. and Lapalme, G. (2009). A systematic analysis of performance measures for classification tasks. *Information Processing & Management*, 45(4), 427–437. doi:10.1016/j.ipm.2009.03.002.

Southwick, D. (1993). Using full spectrum plots. *Orbit*, 14(4).

Southwick, D. (1994). Using full spectrum plots part 2. *Orbit*, 15(2).

Wei, Li, Xu, and Huang (2019). A review of early fault diagnosis approaches and their applications in rotating machinery. *Entropy*, 21(4), 409. doi:10.3390/e21040409.